

Roles of Photon Scattering in Synchrotron X-ray Radiography of In Operando Visualizations of the Polymer Electrolyte Membrane Fuel Cell

N. Ge^a, S. Chevalier^a, J. Hinebaugh^a, M. G. George^a, J. Lee^a, R. Banerjee^a, H. Liu^a, D. Muirhead^a, P. Shrestha^a, and A. Bazylak^a

^aThermofluids for Energy and Advanced Materials (TEAM) Laboratory,
Department of Mechanical & Industrial Engineering, University of Toronto,
Toronto, Ontario M5S 3G8, Canada

A numerical model was developed to predict the attenuated component and the undesired scattered component in the measured X-ray intensity during water visualizations using synchrotron X-ray radiography. The scattering component was found to increase as a function of water thickness traversed by the X-ray beam, and this led to a decrease in the calibrated attenuation coefficient. Due to this relationship between the scattering component and the water thickness, a small water thickness range was demonstrated to produce highly representative attenuation coefficients that resulted in the improved accuracy of water quantifications. Therefore, it was recommended that the calibrated attenuation coefficient should be obtained based on a water thickness range that most appropriately matches the expected liquid water thickness in an operating polymer electrolyte membrane fuel cell.

Introduction

Operating polymer electrolyte membrane (PEM) fuel cells at high current densities is a strategy for achieving effective catalyst utilization and mitigating the cost of power production (1). However, high current density operation corresponds to high rates of water production, and excess liquid water can lead to flooding and poor performance. Therefore, effective water management is an important design objective for the PEM fuel cell.

Synchrotron X-ray radiography, with its high spatial and temporal resolutions, has been used as an in situ diagnostic tool to directly visualize the in operando liquid water transport in PEM fuel cells (2-13). During X-ray radiographic visualizations, in operando images of the fuel cell with the presence of liquid water are termed *wet-state* images. At each pixel of a collected wet-state image, the cumulative water thickness along the X-ray path, t_w [cm], is quantified using the following relationship (14), which was from the Beer-Lambert law:

$$t_w \cdot \mu_{at,w} = \ln \left(\frac{I_{m,dry}}{I_{m,wet}} \right) \quad [1]$$

where $\mu_{at,w}$ is the linear attenuation coefficient of liquid water for monoenergetic X-ray beam [cm^{-1}], $I_{m,dry}$ is the measured attenuated intensity of a reference *dry-state* image

with the absence of liquid water, and $I_{m,wet}$ is the measured attenuated intensity of the wet-state image.

The accuracy in water thickness from Equation 1 relies on the accuracies of the measured attenuated intensities of $I_{m,dry}$ and $I_{m,wet}$. Ideally, the change of intensity from $I_{m,dry}$ to $I_{m,wet}$ should strictly be attributed to the attenuation of the presence of liquid water (with a thickness of t_w). Image processing techniques (15, 16) have been developed to correct measured intensities. Hinebaugh et al. (15) determined that the vertical position of the incident beam oscillated with a significant amplitude of 25 μm , which resulted in an image artifact of false water thickness. Therefore, they employed an image processing technique to pair the dry-state and wet-state images with the same vertical beam position, which effectively eliminated the image artifact. Ge et al. (16) reported that the micrometer-scale movement of the imaged sample led to false water thickness measurements. Hence, they created an image processing technique to determine the distances moved by the sample, and they corrected the movement by translating the images to one common reference location.

The correct use of the attenuation coefficient in Equation 1 is critical for obtaining accurate water thicknesses. The theoretical linear attenuation coefficients, published by the National Institute of Standards and Technology (NIST) (17), is defined as the probability per unit length that an X-ray photon with a known photon energy will interact with atoms in the bombarded material (18). Therefore, the measured attenuated intensities of the dry-state and wet-state images should only be attributed to the X-ray photons that transmit through the imaged sample without any interaction (absorption or scattering). In addition, the incident photons need be monoenergetic in order to result in a constant attenuation coefficient.

However in practice, the measured intensity is attributed to the attenuated beam and the scattered beam. In traversing the imaged sample, the incident X-ray photons are scattered when they are redirected from their original direction by electrons in the sample. The travel direction of the scattered photon with respect to the original direction, termed as the scatter angle, is unpredictable. Therefore, the portion of scattered photons that travel towards the scintillator are unintentionally measured and contribute to the measured attenuated intensities, $I_{m,dry}$ and $I_{m,wet}$. Thus in Equation 1, the theoretical attenuation coefficient is insufficient for establishing the relationship between the two measured intensities, which consist of both the attenuated and scattered components.

In practice, the measured intensity may also contain attenuated and scattered components from harmonic photons. Harmonic photons are introduced to the incident beam by the double-crystal monochromator at a synchrotron beamline. The monochromator selects photons with the desired energy, termed the *fundamental energy*, from the synchrotron white beam (a wide spectrum of photon energies). The selection is based on Bragg's law for X-ray diffraction from a crystal lattice; however, unintentional harmonic photons that satisfy the same selection criterion may also pass the monochromator. Contaminating harmonic photons are exhibited by lower probabilities of sample interaction, i.e. lower attenuation coefficients. Therefore, the associated attenuated and scattered intensities, which were unintentionally measured by the scintillator, lead to an erroneous interpretation of Equation 1 when the theoretical attenuation coefficient of the fundamental energy is used.

As we reported previously (16), directly applying the theoretical attenuation coefficient in Equation 1 leads to an underestimation of liquid water by up to 18.9%. The inaccuracy can be attributed to the undesired components in the measured intensities: the scattered component due to the fundamental photons, the attenuated and the scattering components due to the harmonic photons. Accounting for the scattering and harmonic effects, a calibration experiment was developed in (16) to determine a constant calibrated attenuation coefficient to replace the theoretical value in Equation 1. A custom calibration device with water thicknesses ranging from 0 to 1.6 cm was used. However, the calibrated attenuation coefficient of a homogeneous material was observed to decrease as a function of sample thickness due to either the scattered component (19) or the harmonic component (20) in the measured intensity. Hence, a constant calibrated attenuation coefficient would inevitably lead to inaccurate water thickness calculations. The impact of using a constant calibrated attenuation coefficient on the inaccuracy of calculated water thicknesses must be determined.

Numerical models have been developed for distinguishing the contributions of scattering and harmonics to the attenuated intensity of fundamental energy in the measured intensities. Tran and co-workers developed numerical models to determine the quantities of scattered components (19) and harmonic components (20) in their experimentally measured intensities at a synchrotron beamline. During their measurements, the incident beam and attenuated beam intensities were measured with the use of an ion chamber at the upstream and an ion chamber at the downstream, respectively. It was found that at the fundamental energy of 5 keV, the fraction of the third harmonic component increased from 1.36% (after the monochromator) to 74.5% (after the components of the beamline) due to the large adsorption difference between the photons of fundamental and harmonic energies. However during in situ PEM fuel cell visualization experiments, only the downstream attenuated X-ray photon intensity can be measured. Therefore, a numerical model is needed for determining the scattering and harmonic components for water visualization during in situ PEM fuel cell X-ray radiography experiments.

In this work, a numerical model was developed to determine the fraction of scattering component in the measured intensity from the images obtained from water visualization experiments based on synchrotron X-ray radiography. The inaccuracy of the calculated water thickness was investigated when a constant calibrated attenuation coefficient was used. Specifically, the effect of the water thickness range on the accuracy of the calculated water thickness was studied.

Methodology

In this section, the X-ray radiography experimental setup at the synchrotron beamline is introduced. The custom-made calibration device for holding known thicknesses of liquid water is presented. Then, experimental protocols for obtaining the measured attenuated intensities are described. The numerical model of determining the attenuated and the scattered components is also described.

Synchrotron X-ray radiography imaging setup

X-ray radiography was performed at the Biomedical Imaging and Therapy Bending Magnet (BMIT-BM) 05B1-1 beamline at the Canadian Light Source synchrotron facility in Saskatoon, Canada (21). Figure 1a shows the schematic of the main components at the beamline for obtaining the desired collimated monochromatized beam from the bending magnet white beam.

A metal filter (as shown in Figure 1a), consisting of one single-layered metal sheet, was used to eliminate the low-energy X-ray photons in the white beam. The filter prevents the beamline components from absorbing an excessive amount of heat, and this filtration was achieved by the high attenuation coefficient of the metal at the low photon energies. An aluminum filter with an effective thickness of 0.1103 cm was used in this study. Figure 2 shows the photon flux (a measurement of the beam intensity) as a function of energy level for the white beam and the filtered beam. The recommended energy range by the beamline is 15-40 keV using the aluminum filter, resulting in a remaining flux of 2×10^{12} photons/s/mr²/0.1% bw.

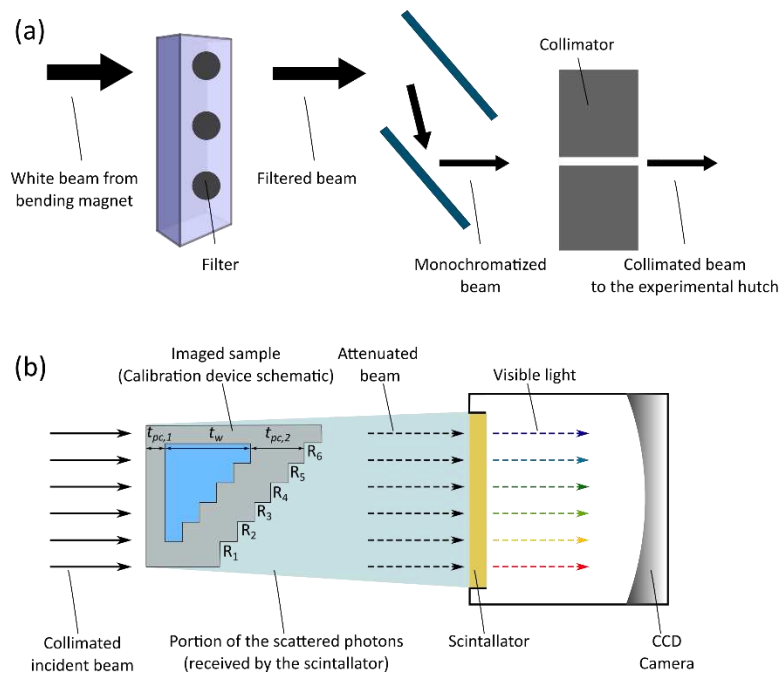


Figure 1. Schematics of the synchrotron radiography setup: (a) in the optics hutch and (b) in the experimental hutch with the calibration device, ex situ PC, as imaged sample.

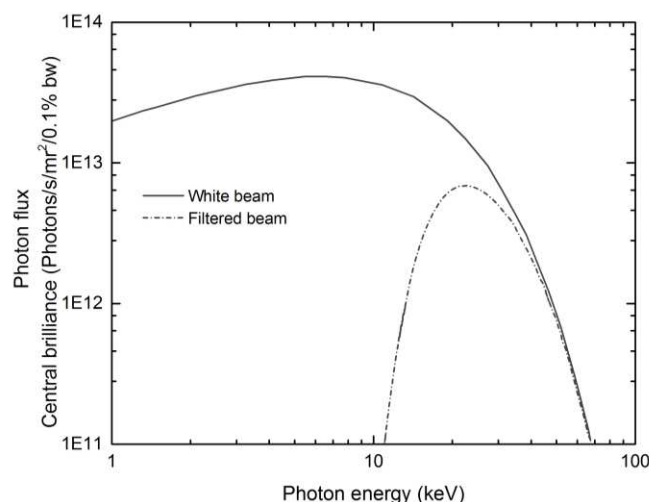


Figure 2. Photon fluxes over the energy spectrum at the (BMIT-BM) 05B1-1 of the white beam from the bending magnet and the filtered beams with a 1-mm aluminum filter (effective thickness of 0.1103 cm).

A Si(2,2,0) double-crystal monochromator was used to select the fundamental beam energy based on Bragg's law for X-ray diffraction from a crystal lattice. The monochromatized beam from the Si(2,2,0) crystals consists of photons of fundamental energy and potentially second- and higher-order harmonic photons. The monochromatized beam was then collimated to produce a parallel beam.

In the experimental hutch (as shown in Figure 1b), the incident beam was attenuated by the imaged sample. An AA-40 scintillator (Hamamatsu Photonics KK) was used to detect the X-ray beam after the beam was attenuated with the imaging sample. The scintillator converted the X-ray photons into visible light. Then, a C11440-22CU CCD camera (Hamamatsu Photonics KK) was used to capture the image from the scintillator. The pixel resolution of the obtained images was 6.5 μm , and the temporal resolution was 3 s.

Calibration device

The custom calibration device, the ex situ PC as shown in Figure 1b, was made of polycarbonate (PC). This device consisted of a single water reservoir, which held six known water thicknesses along the X-ray beam direction ($t_{w,R1}$, $t_{w,R2}$, ..., $t_{w,R6}$). The water thickness range was selected to correspond with the expected water thickness range in the custom fuel cell developed by our group. The dimensions of the device are summarized in Table I.

TABLE I. Geometry parameters of the calibration device.

	Symbol	Value
Dimensions of the calibration device (cm)	$t_{w,R1}$	0
	$t_{w,R2}$	0.305
	$t_{w,R3}$	0.622
	$t_{w,R4}$	0.940
	$t_{w,R5}$	1.257
	$t_{w,R6}$	1.575
	$t_{pc,1}$	1.291
	$t_{pc,2}$	2.560

The theoretical attenuation coefficients of materials in the calibration devices are presented in Table II, which were obtained from published databases (22, 23). Within a unit X-ray pathlength, μ_{at} is the total linear attenuation coefficient, which is the sum of coefficients of the atomic photoelectric effect, μ_{pe} , incoherent scattering, μ_{inc} , and coherent scattering, μ_{coh} . The total scattering coefficient used in this study, μ_{sc} , is the sum of the incoherent and coherent scattering coefficients ($\mu_{inc} + \mu_{coh}$), which describes the probability of a photon being scattered within a unit X-ray pathlength.

TABLE II. Theoretical linear attenuation coefficients from NIST at energy levels of 22, 24, and 40 keV.

	22 keV	24 keV	40 keV
$\mu_{at,w}$	0.656	0.549	0.268
$\mu_{sc,w}$	0.256	0.248	0.211
$\mu_{at,PC}$	0.523	0.455	0.270
$\mu_{sc,PC}$	0.277	0.270	0.235

Experimental protocol

In this section, the energy setting of the three conducted X-ray radiography experiments is explained. The image acquisition and processing procedures are also described.

Energy setting. X-ray radiography experiments were performed in the absence of harmonic photons at the selected fundamental energies above 20 keV. The fundamental photon energies for the three conducted experiments were: 22 keV for Experiment I, 24 keV for Experiment II, and 40 keV for Experiment III. The measured intensities from these experiments can be predicted in terms of the attenuated component and the scattered component of the fundamental energy.

Image acquisition and processing. A sequence of dry-state images, dark-field images, and wet-state images were obtained during each experiment. Dry-state images were obtained when the water reservoir of the calibration device was free of liquid water, and dark-field images were obtained when the incident beam (directed into the experimental hutch) was blocked by a photon shutter. Wet-state images were obtained when the reservoirs in the calibration devices were filled with liquid water. For both the dry-state and wet-state images, image processing steps were taken to eliminate the dark-current noise and to correct for the time-dependent intensity change of the incident beam, as described thoroughly in our previous works (15, 16). Finally, for each known water thickness, the

attenuation ratio of the dry-state image to the wet-state image was obtained: $\ln\left(\frac{I_{m,dry}}{I_{m,wet}}\right)$, where $I_{m,dry}$ and $I_{m,wet}$ are the measured intensities of the dry-state image and wet-state image, respectively.

Scattering model

The measured intensity at the scintillator consisted of the attenuated component and the scattered component of the fundamental energy. The attenuation ratio, $\ln\left(\frac{I_{m,dry}}{I_{m,wet}}\right)$, can be expressed by:

$$\ln\left(\frac{I_{m,dry}}{I_{m,wet}}\right) = \ln\left(\frac{I_{at,dry} + I_{sc,dry}}{I_{at,wet} + I_{sc,wet}}\right) \quad [2]$$

where the subscripts “dry” and “wet” indicate a dry-state image and a wet-state image, respectively. I_{at} is the attenuated beam intensity. Based on the Beer-Lambert law, the attenuated intensities for the dry-state image and the wet-state image can be expressed as:

$$I_{at,dry} = I_0 \cdot \exp[-\mu_{at} \cdot (t_{pc,1} + t_{pc,2})] \quad [3]$$

$$I_{at,wet} = I_0 \cdot \exp[-\mu_{at} \cdot (t_{pc,1} + t_{pc,2}) - \mu_{at,w} \cdot t_w] \quad [4]$$

where, I_0 is the incident beam intensity, μ_{at} [cm^{-1}] the linear attenuation coefficient of the material, and t [cm] is the material thickness traversed by the beam.

In Equation 2, I_{sc} is attributed to the part of the scattered photons that travels towards the scintillator direction, which can be expressed as follows:

$$I_{sc,d} = P \cdot \frac{\mu_{sc,pc}}{\mu_{at,pc}} \cdot I_0 \cdot [1 - \exp(-\mu_{at,pc} \cdot t_{pc,1} - \mu_{at,pc} \cdot t_{pc,2})] \quad [5]$$

$$\begin{aligned} I_{sc,w} = & P \cdot \left\{ \frac{\mu_{sc,pc}}{\mu_{at,pc}} \cdot I_0 \cdot [1 - \exp(-\mu_{at,pc} \cdot t_{pc,1})] + \right. \\ & \frac{\mu_{sc,w}}{\mu_{at,w}} \cdot I_0 \cdot \exp(-\mu_{at,pc} \cdot t_{pc,1}) [1 - \exp(-\mu_{at,w} \cdot t_w)] + \\ & \left. \frac{\mu_{sc,pc}}{\mu_{at,pc}} \cdot I_0 \cdot \exp(-\mu_{at,pc} \cdot t_{pc,1} - \mu_{at,w} \cdot t_w) [1 - \exp(-\mu_{at,pc} \cdot t_{pc,2})] \right\} \quad [6] \end{aligned}$$

where P is the percentage of the scattered intensity measured by the scintillator to the total amount of scattered intensity, and $I_0 \cdot [1 - \exp(-\mu_{at,pc} \cdot t_{pc,1} - \mu_{at,pc} \cdot t_{pc,2})]$ is the intensity loss due to the attenuation of the dry calibration device, which is composed of polycarbonate with a thickness of $(t_{pc,1} + t_{pc,2})$. In (19), the ratio of the Rayleigh scattering attenuation coefficient to the total attenuation coefficient, $\frac{\mu_{coh}}{\mu_{at}}$, was used to calculate the ratio of coherently scattered photons to the total intensity loss. Similarly, in Equations 5 and 6 $\frac{\mu_{sc}}{\mu_{at}}$ is the ratio of the intensity loss due to scattering to the total intensity loss. Hence in Equation 6, the first and third terms inside the braces represent the total scattered

intensity by the solid materials (PC) with lengths $t_{pc,1}$ and $t_{pc,2}$, respectively. The second term inside the braces represents the total scattered intensity by the water.

In Equations 5 and 6, for each experiment a solution for P was obtained through a non-linear least-squares curve fitting (24). Specifically, a temporal value was assigned to P , and the vertical deviation of each region was determined:

$$\chi = \ln \left(\frac{I_{m,dry}}{I_{m,wet}} \right)_{meas} - \ln \left(\frac{I_{m,dry}}{I_{m,wet}} \right)_{mod} \quad [7]$$

where the subscript “*meas*” indicates that the value was obtained from the experiment measurement and the subscript “*mod*” indicates the value was obtained using the model presented in Equation 2 with the assigned value P . For each water thickness value, the least square criterion was defined as the sum of the squares of the vertical deviations:

$$C = \sum (\chi^2)_j \quad [8]$$

where the subscript “*j*” represent the number of known water thicknesses for each experiment (e.g. $j = 5$ for the calibration device with the exclusion of water thickness of 0 cm). The best fit value for P was found until the criterion, C , reached a minimum value.

Results and Discussion

Quantification of the scattered component

The experimentally measured attenuation ratios are shown in Figure 3 as a function of water thicknesses for Experiments I-III. The standard deviations of the measured attenuation ratios were in the range of 0.004-0.008. The curves were fit using the analytical scattering model. Excellent agreement was observed when comparing the experimental data and model predictions. Therefore, the model can be used to predict the attenuation ratio, $\ln \left(\frac{I_{m,dry}}{I_{m,wet}} \right)$, between the dry-state and wet-state images.

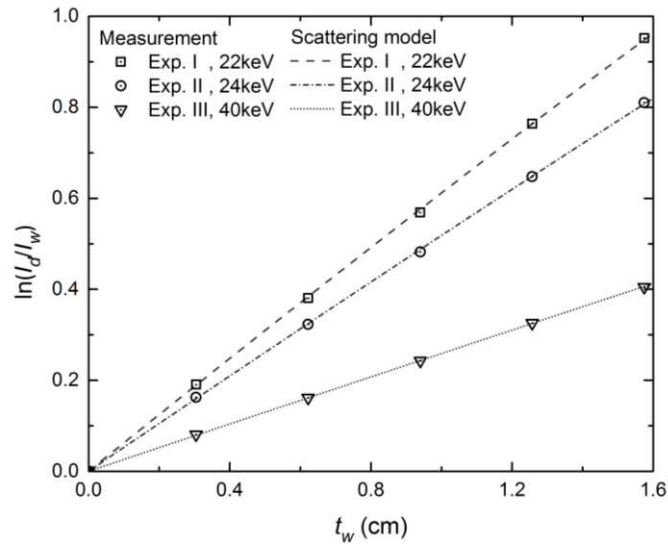


Figure 3. The measured and modeled attenuation ratios between the dry-state image and the wet-state image as a function of the water thickness for Experiments I-III.

The modeled fractions of the scattered component in the measured intensity for Experiments I-III, i.e. f_{sc} , are presented in Figure 4. When the device did not contain liquid water, the scattered component was relatively minor (up to 4.9% at 22 keV). The solid material (composition and dimensions) traversed by the beam (PC) was selected in order to minimize its interactions with the X-ray photons. Its low attenuation coefficient (Table II) led to the low contribution of scattered photons.

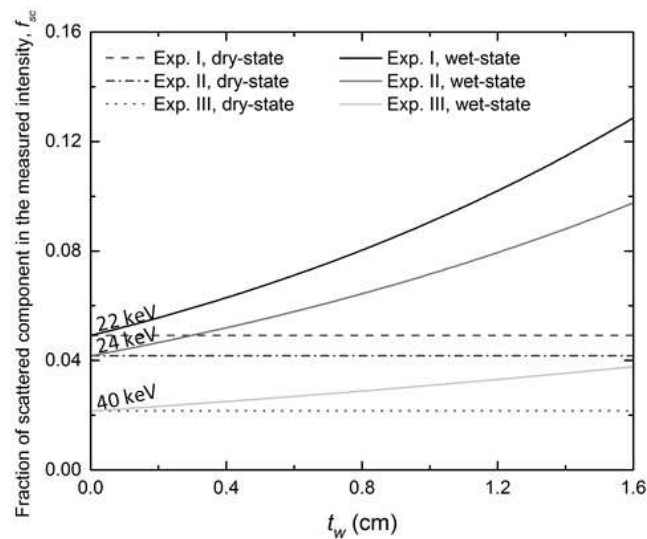


Figure 4. The calculated fractions of the scattering components in the measured beam intensity for the dry-state image and the wet-state image.

In Figure 4, the fraction of the scattered intensity increased as a function of the water thickness, and this result can be explained by the Beer-Lambert law. The Beer-Lambert law is based on the theory that the probability for an X-ray photon to interact with a material (attenuation) increases with increasing material thickness. Correspondingly, the number of

photons that traveled through the material without any interactions, i.e. the dominating attenuated component, decreases exponentially with increasing water thickness (Equation 4). On the other hand, with increasing water thickness the amount of photons scattered by the water increased. Subsequently, the number of photons traveled through the next solid material ($t_{pc,2}$ in Figure 1b) decreased, which led to a decrease of the scattered photons by that portion of the solid material. By observation of Equation 6, the overall change of scattered intensity with respect to water thickness increase was minimal. In summary, with increasing water thickness the attenuated component, $I_{at,wet}$, and the measured intensity, $I_{m,wet}$, decreased, whereas the fraction of the scattered component increased.

In Figure 4, the fraction of the scattered component was observed to decrease as the photon energy increased. Attenuation coefficients also decreased with increasing photon energy (Table II), which is attributed to the increasing likelihood that higher energy photons can penetrate the material in the absence of scattering or absorption. As a result, at high proton energies, photons exhibit a higher probability of reaching the scintillator, and the attenuated component in the measured intensity is relatively high while the scattered component is relatively low.

Effect of scattering on the calibrated attenuation coefficient

The calibrated attenuation coefficient was determined for each water thickness, and the corresponding attenuation ratio was predicted from the following equation:

$$\mu_{at,w}^{cali} = \frac{\ln\left(\frac{I_{m,dry}}{I_{m,wet}}\right)_{mod}}{t_w} \quad [9]$$

where t_w is a known water thickness, and $\ln\left(\frac{I_{m,dry}}{I_{m,wet}}\right)_{mod}$ is the attenuation ratio obtained from the scattering model. A comparison between our calibrated attenuation coefficients (as a function of water thickness) for Experiments I-III and the theoretical NIST water attenuation coefficients, $\mu_{at,w}$ from Table II, are presented in Figure 5. The calibrated water attenuation coefficients were lower than the theoretical NIST values. For near zero water thicknesses, the measured intensities of the dry-state and wet-state images exhibited nearly equivalent scattered components (see Figure 4 at $t_w = 0$). The calibrated attenuation coefficient from Equation 9 can be expressed in terms of the attenuated and scattered components as follows:

$$\mu_{at,w}^{cali} = \frac{\ln\left\{\frac{I_0 \cdot \exp[-\mu_{at} \cdot (t_{pc,1} + t_{pc,2})] + I_{sc,dry}}{I_0 \cdot \exp[-\mu_{at} \cdot (t_{pc,1} + t_{pc,2}) - \mu_{at,w} \cdot t_w] + I_{sc,wet}}\right\}}{t_w}, \quad [10]$$

where $I_{sc,dry} = I_{sc,wet}$ for $t_w \cong 0$

The theoretical NIST attenuation coefficient is expressed without the scattered components as follows:

$$\mu_{at,w} = \frac{\ln\left\{\frac{I_0 \cdot \exp[-\mu_{at} \cdot (t_{pc,1} + t_{pc,2})]}{I_0 \cdot \exp[-\mu_{at} \cdot (t_{pc,1} + t_{pc,2}) - \mu_{at,w} \cdot t_w]}\right\}}{t_w} \quad [11]$$

Since the theoretical NIST attenuation coefficient does not take scattering into account ($I_{sc,dry}$ and $I_{sc,wet}$), the resulting values of $\mu_{at,w}$ are expected to be less than that of the calibrated attenuation coefficients from Equation 10. With increasing water thickness, the attenuated intensity in the wet-state image, $I_{at,wet}$, decreased exponentially, whereas the change in the scattered component, $I_{sc,wet}$, was insignificant. By observation of Equation 10, the calibrated water attenuation coefficient decreases as a function of increasing water thickness, and as a result the calibrated water attenuation coefficient diverges from the theoretical NIST value. Since photon scattering becomes less pronounced at higher energies, the impact of scattering becomes less pronounced at these higher energies. As shown in Figure 5, the calibrated attenuation coefficient at 22 keV decreased by 3.6% between a water thickness of $t_w = 0$ cm and $t_w = 1.6$ cm, whereas, at 40 keV the calibrated attenuation coefficient decreased by only 0.8%.

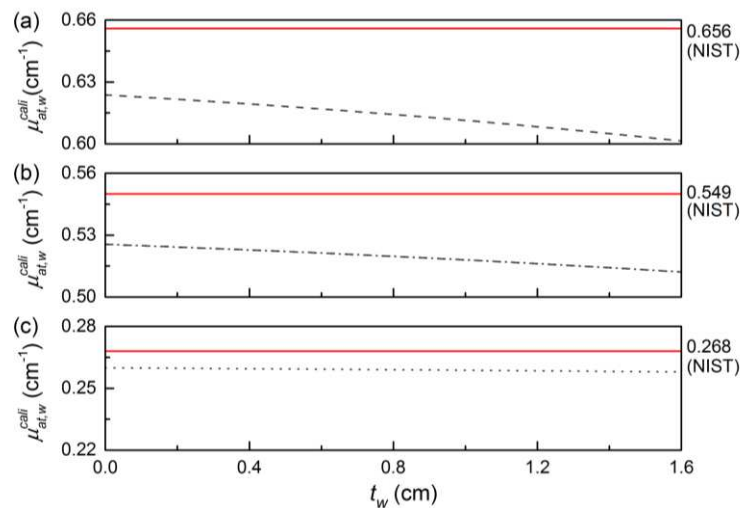


Figure 5. The calibrated attenuation coefficient for liquid water based on a single water thickness for (a) Experiment I (22 keV), (b) Experiment II (24 keV), and (c) Experiment III (40 keV). The theoretical value for each experiment is presented as a horizontal line in each graph, respectively.

Effect of water thickness range on the accuracy of water quantification

As shown in Figure 5, the calibrated attenuation coefficient is a function of the water thickness due to photon scattering. In this section, we present the effect of the water thickness range on the accuracy of the calculated water thicknesses.

Calibrated attenuation coefficients were determined from the gradient of the linear-fit line over various selected water thickness ranges from Experiment II in Figure 3. For example, $\mu_{at,w}^{cali,0.4}$ was obtained based on the curve in the water thickness range of 0 - 0.4 cm. During water quantification calculations with $\mu_{at,w}^{cali,0.4}$, the calculated water thickness, $t_{w,calc}$, was determined by applying the attenuation ratio obtained from the scattering model, $\ln\left(\frac{I_{m,dry}}{I_{m,wet}}\right)_{mod}$, and $\mu_{at,w}^{cali,0.4}$ into Equation 1. Based on the scattering model, each attenuation ratio corresponds to a known water thickness, $t_{w,known}$. Therefore, the percentage discrepancy between the known water thickness and the calculated water

thickness, i.e. $\frac{t_{w,calc} - t_{w,known}}{t_{w,known}}$, was obtained and presented as a function of the known water thickness in Figure 6. On this figure, the water thickness ranges and the related constant attenuation coefficients are presented in the legend.

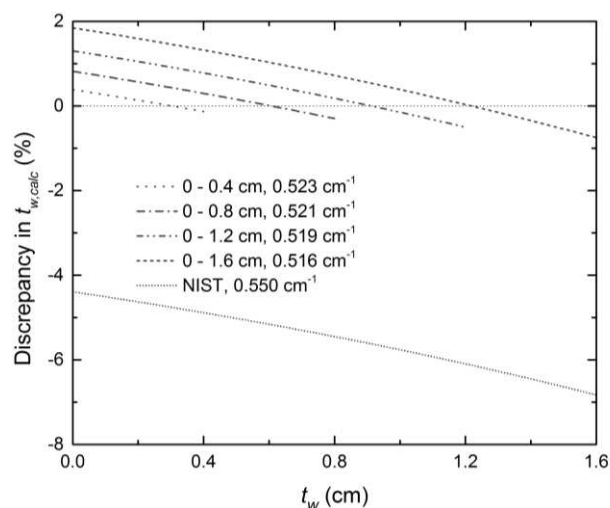


Figure 6. The calculated percentage discrepancy between the known water thickness and the calculated water thickness based on the calibrated water attenuation coefficients from a range of water thicknesses. The discrepancy by using the theoretical value from NIST was also presented.

When the theoretical NIST water attenuation coefficient was used, large discrepancies (between -4.4 and -6.8%) in the calculated water thicknesses were observed (Figure 6). These large inaccuracies stem from the inappropriate use of the theoretical NIST attenuation coefficient when scattered photons are present. In contrast, the calibrated attenuation coefficient greatly reduced the inaccuracy (by up to 1.8%). The inaccuracy was further reduced as the calibration water thickness range decreased. For example, the inaccuracy was reduced from 1.8% to 0.4% when the calibration range was reduced from 0 - 1.6 cm to 0 - 0.4 cm. As the water thickness range decreased, the difference in the fraction of scattered component decreased as shown in Figure 4. Hence in Figure 5b, the small calibration water thickness range was observed to lead to a small variance in the calibrated attenuation coefficient, which made a constant calibrated attenuation coefficient more suitable. Therefore for water quantification purposes (e.g. in situ PEM fuel cell experiment), the calibrated attenuation coefficient should be obtained based on a water thickness range that is most appropriately matched to the expected thickness in the fuel cell.

Conclusions

In this work, we developed and presented a numerical model to simulate the scattered component contribution to the measured beam intensity during liquid water visualizations with synchrotron X-ray radiography. The scattered component increased as the water thickness increased, and this relationship resulted in the decrease of the calibrated attenuation coefficient. We demonstrated that a small range of water thickness during the calibration experiment decreases the inaccuracy of the calculated water thickness. In order to obtain a highly representative attenuation coefficient, we recommend to calibrate the

water attenuation coefficient from a water thickness range that closely matches the range of water thickness expected inside the fuel cell.

Acknowledgments

Financial support from the Natural Sciences and Engineering Research Council of Canada (NSERC), the NSERC Discovery Accelerator Program, the NSERC Canada Research Chairs Program, the Ontario Ministry of Research and Innovation Early Researcher Award, and the Canada Foundation for Innovation are gratefully acknowledged. The authors acknowledge Dr. George Belev, Dr. Adam Webb, Dr. Tomasz Wysokinski, and Dr. Ning Zhu at the Canadian Light Source for their generous assistance. Research described in this paper was performed at the Canadian Light Source, which is funded by the Canada Foundation for Innovation, the Natural Sciences and Engineering Research Council of Canada, the National Research Council Canada, the Canadian Institutes of Health Research, the Government of Saskatchewan, Western Economic Diversification Canada, and the University of Saskatchewan.

References

1. Y. Tabuchi, T. Shiomi, O. Aoki, N. Kubo and K. Shinohara, *Electrochim. Acta.*, **56**, 1 (2010).
2. C. Hartnig and I. Manke, in *Encyclopedia of Electrochemical Power Sources*, J. Garche, Editor, p. 738, Elsevier, Amsterdam (2009).
3. J. Hinebaugh, J. Lee and A. Bazylak, *J. Electrochem. Soc.*, **159** (12) (2012).
4. J. Haussmann, H. Markoetter, R. Alink, A. Bauder, K. Dittmann, I. Manke and J. Scholta, *J. Power Sources.*, **239** (2013).
5. F. N. Büchi, R. Flückiger, D. Tehlar, F. Marone and M. Stampanoni, *ECS Trans.*, **16**, 2 (2008).
6. P. Antonacci, S. Chevalier, J. Lee, N. Ge, J. Hinebaugh, R. Yip, Y. Tabuchi, T. Kotaka and A. Bazylak, *Electrochim. Acta.*, **188** (2016).
7. P. Antonacci, S. Chevalier, J. Lee, R. Yip, N. Ge and A. Bazylak, *Int. J. Hydrogen Energy.*, **40**, 46 (2015).
8. J. Hinebaugh, J. Lee, C. Mascarenhas and A. Bazylak, *Electrochim. Acta.*, **184** (2015).
9. S. Chevalier, N. Ge, J. Lee, P. Antonacci, R. Yip, M. G. George, H. Liu, R. Banerjee, M. Fazeli and A. Bazylak, *Electrochemistry Communications.*, **59** (2015).
10. J. Lee, R. Yip, P. Antonacci, N. Ge, T. Kotaka, Y. Tabuchi and A. Bazylak, *J. Electrochem. Soc.*, **162**, 7 (2015).
11. J. Lee, J. Hinebaugh and A. Bazylak, *J. Power Sources.*, **227** (2013).
12. I. Manke, C. Hartnig, M. Gruenerbel, W. Lehnert, N. Kardjilov, A. Haibel, A. Hilger, J. Banhart and H. Riesemeier, *Appl. Phys. Lett.*, **90**, 17 (2007).
13. Chevalier, S., Lee, J., Ge, N., Yip, R., Antonacci, P., Tabuchi, Y., Kotaka, T., Bazylak, A., *Electrochim. Acta.*, **210** (2016).
14. S. Lee, S. Kim, G. Park and C. Kim, *Int. J. Hydrogen Energy.*, **35**, 19 (2010).
15. J. Hinebaugh, P. R. Challa and A. Bazylak, *J. Synchrotron Rad.*, **19** (2012).
16. N. Ge, S. Chevalier, J. Hinebaugh, R. Yip, J. Lee, P. Antonacci, T. Kotaka, Y. Tabuchi and A. Bazylak, *J. Synchrotron Rad.*, **23**, 2 (2016).
17. J. H. Hubbell and S. M. Seltzer, *Table of X-ray mass attenuation coefficients and mass energy-absorption coefficients 1 keV to 20 MeV for elements Z= 1 to 92 and*

- 48 additional substances of dosimetric interest.*, NIST-PL. Ionizing Radiation Div. (1995).
18. J. H. Hubbell, *Photon Cross Sections, Attenuation Coefficients and Energy Absorption Coefficients from 10 keV to 100 GeV (No. NSRDS-NBS-29).*, National Standard Reference Data System (1969).
 19. C. Tran, M. De Jonge, Z. Barnea and C. Chantler, *Journal of Physics B: Atomic, Molecular and Optical Physics.*, **37**, 15 (2004).
 20. C. Tran, Z. Barnea, M. De Jonge, B. Dhal, D. Paterson, D. Cookson and C. Chantler, *X-Ray Spectrometry.*, **32**, 1 (2003).
 21. T. W. Wysokinski, D. Chapman, G. Adams, M. Renier, P. Suortti and W. Thomlinson, *Nuclear Instruments & Methods in Physics Research Section A-Accelerators Spectrometers Detectors and Associated Equipment.*, **582**, 1 (2007).
 22. M. J. Berger, J. Hubbell, S. Seltzer, J. Chang, J. Coursey, R. Sukumar, D. Zucker and K. Olsen, *XCOM: photon cross sections database.*, NIST Standard Reference Database., **8**, 1 (1998).
 23. J. M. Boone and A. E. Chavez, *Med. Phys.*, **23**, 12 (1996).
 24. D. C. Harris, *J. Chem. Educ.*, **75**, 1 (1998).